DOI: 10.24352/UB.OVGU-2019-005 TECHNISCHE MECHANIK, 39, 1, (2019), 39 – 50
submitted: November 01, 2018

The Influence of Different Arrangements of Shallow Dimples on the Resistance of Plates Subjected to Relative Fluid Motion

J. Praß, H. Wannmacher, J. Franke, S. Becker

Shallow dimples have long been a scientifically investigated topic to reduce the flow resistance of objects subjected to overflow. Most of the investigations on the influence of dimples on flow resistance have so far been carried out experimentally. Although the arrangements and flow conditions are often similar, different research activities conclude differently concerning the effect of the surface structures. This also leads to disagreement regarding the causes of flow resistance reductions. In this paper, time-resolved Large Eddy Simulations on two different, already experimentally investigated setups of dimples have been carried out to better understand the effects of dimples on the surface being subjected to relative fluid motion. In one case the dimples were examined in overlapping arrangement, in the other case in a non-overlapping arrangement. We were able to show that the formation of streaks near the surface significantly influences the local contribution to the flow resistance. For the overlapping arrangement, only a slight resistance reduction of 0.12 % was determined. For the non-overlapping arrangement, the mean resistance reduction was found to be 3.16 %. Regardless of the resistance reduction determined, a clear interaction between longitudinal vortices near the plate and local contributions to flow resistance could be demonstrated. Since these longitudinal vortices are directly influenced by the dimples, it is very likely that an optimized arrangement of the dimples, adapted to the flow conditions, can reduce the resistance.

Nomenclature

A	m^2	wetted area projected parallel to flow direction
C_w	-	WALE constant
D	m	dimple diameter
F_t	$\mathrm{kg\,m\,s}^{-2}$	total resistance force
H	m	height of computational domain
L_s	m	mixing length
R_c	-	correlation coefficient
S_{ij}^d	s^{-2}	traceless symmetric part of the square of the velocity gradient tensor
$\hat{S}_{ij}$	s^{-1}	rate-of-strain tensor for the resolved scale
T	-	dimensionless period time
V	m^3	volume of a cell
c_F, c_{F0}	-	total drag coefficient, total drag coefficient of smooth plate
d	m	distance to the wall
$\hat{g}_{ij}$	s^{-1}	velocity gradient tensor
h	m	dimple depth
l_x	m	streamwise distance
l_z	m	spanwise distance
p	$\mathrm{kg\,m}^{-1}\,\mathrm{s}^{-2}$	pressure
r	m	dimple edge radius
s	m	spacial displacement
s_z	m	spanwise shift
t	s	time
u	$\mathrm{m\,s}^{-1}$	velocity
u, v, w	$\mathrm{m\,s}^{-1}$	velocity components in x, y and z-direction
x, y, z	m	spatial coordinates
y^+	-	dimensionless wall distance
δ_{ij}	-	kronecker delta

Δx^+	-	dimensionless streamwise distance
Δz^+	-	dimensionless spanwise distance
κ	-	von Kármán constant
μ_t	$\mathrm{kg\,m^{-1}\,s^{-1}}$	eddy viscosity
ν	$\mathrm{m^2\,s^{-1}}$	kinematic viscosity
ρ	$\mathrm{kg\,m^{-3}}$	density
τ_w	$\mathrm{kg\,m^{-1}\,s^{-2}}$	wall shear stress
τ_{ij}	$\mathrm{m^2\,s^{-2}}$	sub-grid structure stresses
ξ	m	spatial coordinate
NOL		non-overlapping dimple arrangement
OL		overlapping dimple arrangement
WALE		Wall-Adapting Local Eddy-Viscosity Model

Subscripts and Superscripts

$\bar{\square}$	temporal average of a quantity
$\hat{\square}$	spatially filtered quantity
$\square'$	fluctuating part of a quantity
in	inlet
max	maximum
mean	temporal average
ref	reference
i, j	index
∞	bulk

1 Introduction

Flow-induced resistance in viscous fluids is an important phenomenon that affects the efficiency of many technical systems. A distinction is usually made between form and friction resistance. As friction losses occur wherever fluids of any kind – such as air or water – show relative velocities to walls they interact with, the amount of power expended globally to overcome these losses is significant. While the form resistance is determined by the projected area of a body perpendicular to the direction of the relative movement – i. e. shape and cross-section – friction resistance is mainly dependent on dimension and properties of the surface that is overflown. While form resistance is only important in the case of bodies surrounded by flow, friction resistance plays an important role in both the flow around and through objects. Since the flow resistance of moving objects such as a car or an airplane as well as of fluid transport, for example through pipelines, has to be overcome by means of energy consumption, many research projects deal with investigations on the reduction of resistance.

In order to reduce the frictional resistance active and passive methods exist. Classical active methods are characterised by the fact that the flow near the wall is influenced by actuators in order to keep the flow resistance low. Recent research aims to flatten the velocity profile by increasing the flow velocity near the wall, which destabilizes the turbulence downstream and relaminarizes the flow (Kühnen et al. (2018)). So far, however, this effect could only be observed in pipe flows. Passive methods, such as the use of riblets (e. g. Garcia-Mayoral and Jimenez (2011)), protrusions (e. g. Sirovich and Karlsson (1997)), tabs (e. g. Park et al. (2006)) or grooves (e. g. Krieger et al. (2018)), are aimed at changing the wall geometry or structure in order to also modulate the flow, and thereby decreasing the resistance. The potentials for resistance reduction through active methods such as boundary layer suction (e. g. Antonia et al. (1994)), boundary layer blowing (e. g. Park and Choi (1999)), moving walls (e. g. Baron and Quadrio (1996)) and boundary layer influencing (e. g. Cimarelli et al. (2013)) are higher than with passive methods, but this effect is often relativized in the overall energy balance by the energy consumption of the actuators (Quadrio and Ricco (2004)). In addition, actuators are susceptible to failures, require maintenance and additionally increase the total weight of a system, which is why passive resistance reduction methods are no less important in research.

A promising and controversially debated approach is the use of dimples, which, in addition to reducing drag, offers other advantages such as weight reduction of the system and low sensitivity to pollution (Turow (2012)). Dimples were originally studied in terms of their ability to increase convective heat transfer from walls. While this aspect was intensively examined, only relatively few scientific papers deal with the potential of the drag reduction of dimples (Nesselrooij et al. (2016)). Since the mechanisms responsible for the reduction of drag are not yet fully understood and as various scientists use different test setups, the published results are inconsistent and sometimes

even contradictory. Some scientists found in their investigations only resistance increases (e. g. Lienhart et al. (2008); Lashkov and Samoilova (2002)), while others found reductions of up to 20 % for low Re (Veldhuis and Vervoort (2009)) and 17 % for high Re in experiments (Kiknadze et al. (2012)). However, the results of the authors Kiknadze et al. (2012) are discussed critically, as the experiments and related results could not yet be reproduced and thus validated. Resistance reductions have been demonstrated for dimples with depth to diameter (h/D) ratios of less than 10 % in different arrangements (Nesselrooij et al. (2016); Veldhuis and Vervoort (2009); Tay (2011); Tay et al. (2015)). Tay et al. (2015) discovered in invasive (hot-wire anemometry) experiments that longitudinal vortices introduced by the dimples near the wall have similar effects on drag reduction as active methods. Since these structures depend very strongly on the flow conditions and it is difficult to measure them from a measurement point of view – invasive methods show interactions with the flow, laser-based methods can only be carried out close to the wall with considerable effort – numerical methods are required to investigate the near-wall structures in detail. In this work we therefore use time-resolved Large Eddy Simulations (LES) to examine the effects of two geometries already experimentally investigated by Nesselrooij et al. (2016). Additionally, a flat plate without dimples was simulated with the same mesh resolution and boundary conditions as a reference case in order to compare the results of the dimpled plates with.

2 Numerical Setup

In the present work, all simulations were carried out with Ansys Fluent (v17.2). In order to adequately represent the near-wall flow, an adaptive mesh and a wall-adapting local eddy-viscosity (WALE) model for sub-grid scale structure modeling were used.

2.1 Governing Equations

In Eq. 1 and 2 mass conservation and momentum conservation in filtered, incompressible form are given, respectively.

$$\frac{\partial \hat{u}_j}{\partial x_j} = 0 \tag{1}$$

$$\frac{\partial \hat{u}_j}{\partial t} + \frac{\partial \hat{u}_i \hat{u}_j}{\partial x_i} = -\frac{\partial \hat{p}}{\partial x_j} + \frac{\partial}{\partial x_i}\left(2\nu \hat{S}_{ij}\right) - \frac{\partial \tau_{ij}}{\partial x_i} \tag{2}$$

Here, $\hat{S}_{ij}$ denotes the rate-of-strain tensor for the resolved scale (Eq. 3), ν denotes the kinematic viscosity and τ_{ij} the sub-grid structure stresses that have to be modeled, in the current paper this was done using a WALE model as proposed by Nicoud and Ducros (1999) implemented in Fluent, i. e. the eddy viscosity μ_t is modeled according to Eq. 4,

$$\hat{S}_{ij} = \frac{1}{2}\left(\frac{\partial \hat{u}_j}{\partial x_i} + \frac{\partial \hat{u}_i}{\partial x_j}\right) \tag{3}$$

$$\mu_t = \rho L_s \frac{\left(S^d_{ij} S^d_{ij}\right)^{3/2}}{\left(\hat{S}_{ij}\hat{S}_{ij}\right)^{5/2} + \left(S^d_{ij} S^d_{ij}\right)^{5/4}} \tag{4}$$

where the mixing length L_s and the traceless symmetric part of the square of the velocity gradient tensor S^d_{ij} are defined as in Eqs. 5 and 6, respectively:

$$L_s = \min\left(\kappa d, C_\mathrm{w} V^{1/3}\right) \tag{5}$$

with the von Kármán constant $\kappa = 0.41$, the distance to the wall d, the WALE constant $C_\mathrm{w} = 0.325$ and the

volume of the cell V,

$$S_{ij}^d = \frac{1}{2}\left(\hat{g}_{ij}^2 + \hat{g}_{ji}^2\right) - \frac{1}{3}\delta_{ij}\hat{g}_{kk}^2 \tag{6}$$

with the velocity gradient tensor $\hat{g}_{ij} = \partial\hat{u}_i/\partial x_j$.

2.2 Computational Setup

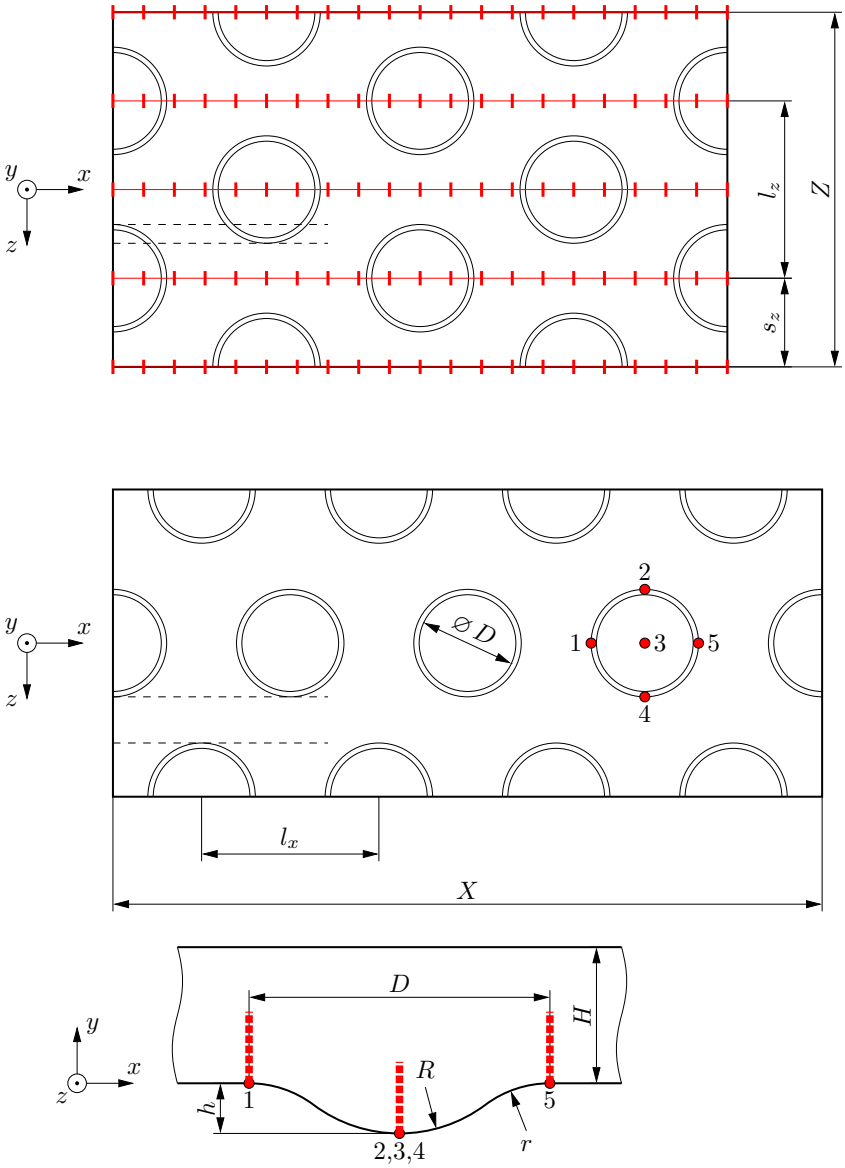

Figure 1: Arrangement and relations of dimples in the domain: overlapping (OL) arrangement with positions of monitor points for correlation analysis indicated (*top*), non-overlapping (NOL) arrangement with positions 1–5 for velocity analysis indicated at an arbitrary dimple (*middle*) and cross-section of a dimple with a path of measurement line for velocity analysis indicated (*bottom*)

To describe the dimples and their arrangement on a surface, six parameters are sufficient: The diameter D, the depth h, edge radius r, streamwise distance l_x, spanwise distance l_z and spanwise shift s_z. In the current paper, two staggered arrangements were used, meaning that $s_z = l_z/2$. In the first arrangement dimples were positioned overlapping (OL), in the second arrangement a non-overlapping (NOL) setup was used. The used setups and mentioned parameters are shown in Fig. 1, the corresponding unit-laden values are given in Tab. 1. The domains have been chosen large enough to be able to capture large-scale structures. The height was set to $H = \max(2\,l_x; 2\,l_z)$.

The dimpled wall was defined as a no-slip wall, the upper wall was defined as free-slip wall in order to simulate a free overflown plate and the boundaries in z-direction and x-direction as translational periodic boundary conditions. The Reynolds number based on dimple diameter $Re = D \cdot u/\nu$ was set via a pressure gradient in x-direction and was fixed at $Re \approx 35\,000$.

Table 1: Geometrical Setup as experimentally investigated by Nesselrooij et al. (2016)

case	D in mm	h/D in %	l_x/D	l_z/D	r/D
OL	20	2.5	2.859	1.650	0.5
NOL	20	2.5	1.650	2.859	0.5

Special attention was paid to the used mesh. To achieve values of $y^+ < 1$ as well as $\Delta x^+ < 10$ and $\Delta z^+ < 10$, the mesh near the wall was refined adaptively as shown in Fig. 2. In every adaptive layer perpendicular to the wall at least four cells were used. With these restrictions, a mesh convergence study was conducted to ensure that the results are not affected by discretization errors.

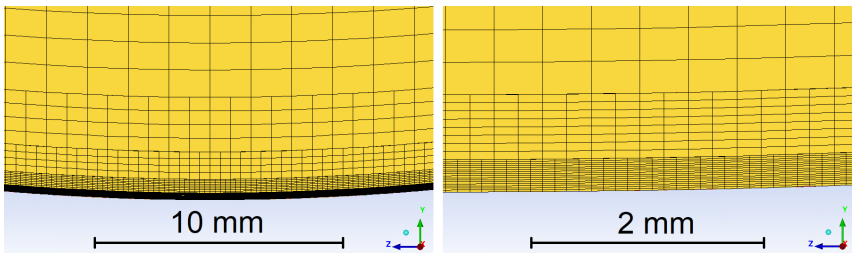

Figure 2: Detail of the computational mesh in direct proximity of a dimple (*left*) and magnified view of boundary layer resolution (*right*)

2.3 Validation

In addition to conditions $y^+ < 1$, $\Delta x^+ < 10$ and $\Delta z^+ < 10$ (Fröhlich (2006)) two other criteria for validation have been taken into account. First, the appropriate resolution of the boundary layer was proven since the correct representation of physical effects in direct proximity of the wall were of major interest. For this purpose, the dimensionless streamwise velocity of the simulation of the non-dimpled channel was compared with literature values of Moser et al. (1999). As shown in Fig. 3 the results are consistent with the literature values, meaning that the physical effects close to wall can well be captured by the conducted LES.

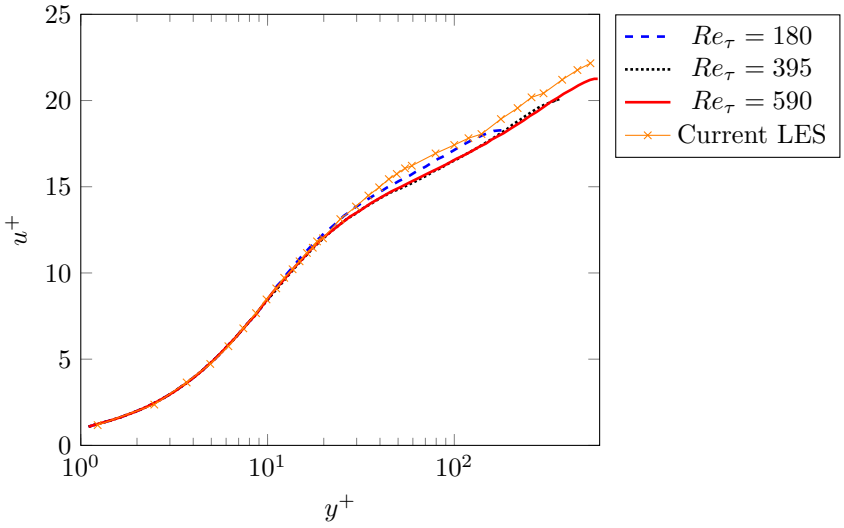

Figure 3: Comparison of boundary layer profile of the current LES with data for turbulent boundary layers by Moser et al. (1999)

Second, it was shown that the domain size is sufficient by considering the correlation coefficient given in Eq. 7 (Herwig and Schmandt (2015)) at different wall distances. According to Kiš et al. (2015) R_c should have a

zero crossing when using periodic boundary conditions, since the correlation naturally increases to unity when approaching the periodic boundary condition and can thus not stay at zero as it is proposed for non-periodic boundary conditions (Fröhlich (2006)). For the correlation analysis, monitor points in four different y^+-ranges were evaluated at five z-values, each with 21 x-values distributed evenly over the entire domain. The x- and z-locations are given in Fig. 1. The positions in y^+-direction were selected such that one measuring path lies in each of the different ranges of the boundary layer. These ranges are i) the viscous sub-layer ($y^+ \lesssim 5$), ii) the buffer-layer ($5 \lesssim y^+ \lesssim 30$), iii) the log-law region ($30 \lesssim y^+ \lesssim 100 \ldots 800$) and iv) the outer layer ($y^+ \gtrsim 1000$). Therefore, y^+-positions 4, 15, 137 and 1073 were chosen. As shown in Fig. 4 R_c reached zero well before $x = 0.4 \cdot X$, which was the same for all z-locations investigated, as well as for the shown average taken over the five paths, indicating that the domain size is chosen big enough to avoid non-physical phenomena stemming from correlated velocity fluctuations.

$$R_\mathrm{c} = \frac{\overline{u'(x,t)\,u'(x+s,t)}}{\sqrt{\left(\overline{u'(x,t)^2}\right)\left(\overline{u'(x+s,t)^2}\right)}} \tag{7}$$

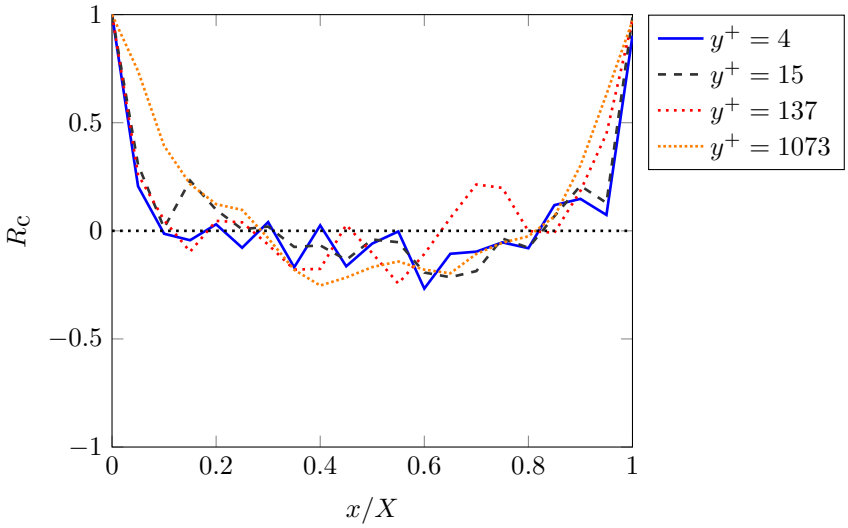

Figure 4: Comparison of correlation coefficient R_c for different y^+-locations averaged over five equally spaced z-positions

All simulations were initialized using results from RANS simulations carried out on the same mesh superimposed with synthetic turbulence in order to accelerate convergence. The bulk velocity u_∞ as well as the pressure p at the periodic boundary condition at $x = 0$ and the maximum velocity u_max at a point just below the free-slip boundary condition were considered to find the point in time at which the flow no longer shows any influence from the initial conditions. Velocities were made dimensionless using bulk velocity u_∞. As no such quantity exists for pressure p, pressure was shifted by its mean value and scaled by reference pressure $p_\mathrm{ref} = 20\,\mathrm{Pa}$. As shown in Fig. 5, the point from which on the quantities fluctuate around a constant value occurs from about ten flow-through times (calculated value: 10.57)[1], which is why averaging was started from this time on. For the non-overlapping arrangement (not shown) time for averaging was reached at 9.16 flow-through times. Each of the simulations took about 70 000 to 72 000 CPU hours to complete.

[1]This is the point from which on fluctuations were so small that all values fulfilled the criteria $|u_\mathrm{in}/u_\infty - 1| \leq 0.15\,\%$.

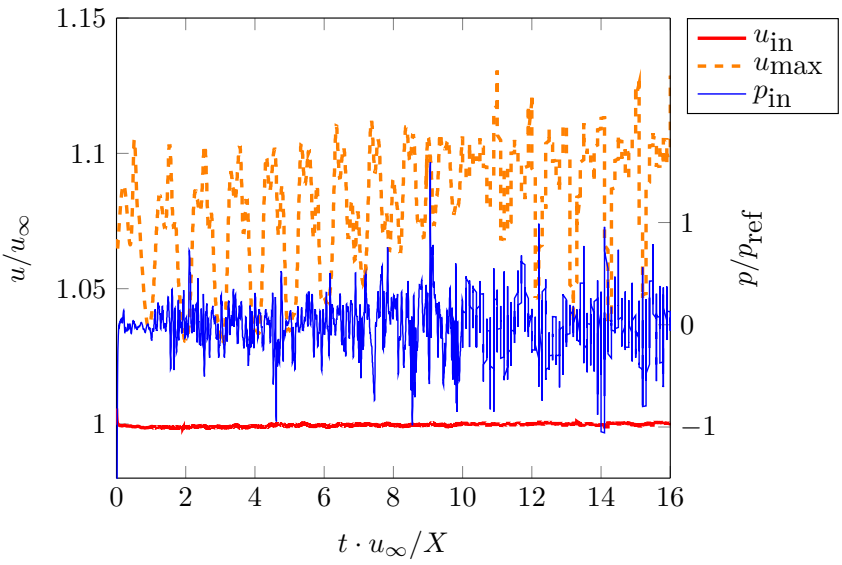

Figure 5: Determination of the statistically averaged state of the LES shown for dimpled plate with overlapping arrangement (OL)

3 Results

3.1 Drag Reduction

The flow resistance of a body subjected to fluid flows is composed of form and friction resistance. Since no wetted, projected surface perpendicular to the direction of flow is present on a smooth, parallel overflowed plate, the component of form resistance vanishes. The total resistance force F_t of the plate is thus determined exclusively by the resulting wall shear stress $\tau_\text{w} = F_\text{t}/A$. The total drag coefficient can be determined according to Eq. 8. The area A is the wetted area projected parallel to the direction of flow, which in the case of the smooth plate is identical to the wetted area. In the case of the dimpled plates, the total resistance force F_t comprises not only the friction component but also the form resistance component. The dimple also increases the wetted surface of the plate. Since the focus of this paper is on influencing the resistance of a surface, the total resistance coefficient c_F according to Eq. 8 using the total resistance force F_t related to area A of the smooth plate was used as a reference value. For the dimpled case, this area corresponds to the wetted area projected parallel to the direction of flow. This type of evaluation took into account all possible influences on the resistance. In addition, the comparability with the results given by Nesselrooij et al. (2016) is improved, since it corresponds to the procedure in their experiments. Fig. 6 shows the ratio of total drag coefficient c_F to drag coefficient of the undimpled plate c_{F0} for the investigated arrangements OL and NOL as well as the time-averaged values indicated by index 'mean'.

$$c_F = \frac{2F_\text{t}}{\rho u_\infty^2 A} \tag{8}$$

It can be seen that – similar to velocity and pressure in Fig. 5 – the values fluctuate around this average value. Interestingly, however, the dimensionless period times T of c_F/c_{F0} are in the range of $T \approx 7 \ldots 8$ flow-through times and are thus considerably longer than those of velocity and pressure fluctuations. The oscillation is furthermore overlaid by higher frequency fluctuations and the amplitudes are higher than those of the average velocity would suggest, but the maximum expansion is still less than 10 %. For arrangement OL at $Re \approx 35\,000$ Nesselrooij et al. (2016) found a drag reduction of approximately 3 %. In the current LES, the reduction in drag observed for this setup was not more than 0.12 % and is therefore hardly existent. Better results concerning drag reduction were obtained with arrangement NOL, where resistance was reduced by as much as 3.16 %. However, Nesselrooij et al. did not find any resistance reduction for this setup, but even a slight increase in resistance of little more than 2 %. From this point of view, the results of the current LES are at first sight not in good agreement with the literature. Since the expected and also the found differences are in the range of single-digit percentages, this fact becomes less pronounced as the difference between simulation and experiment is ≈ 3 % for arrangement OL and ≈ 5 % for

arrangement NOL, while the measurement repeatability was already up to 2 % (Nesselrooij et al. (2016)).

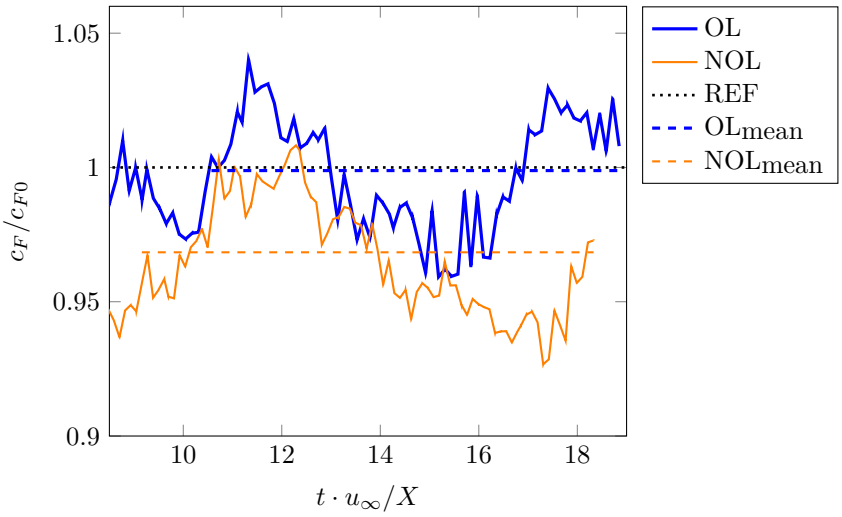

Figure 6: Total drag coefficient c_F for the plate without dimples (REF), plate with overlapping dimple arrangement (OL) and plate with non-overlapping dimple arrangement (NOL) related to c_{F0}

3.2 Flow Structures and Pressure Distribution

Regardless of the actual reduction of resistance, the main focus lies on investigating the physical mechanisms of action that influence the resistance of dimpled surfaces. For this purpose, the flow structures close to the wall are examined in detail below. Fig. 7 (*top*) shows the velocity field in a section plane at $y^+ = 20$. Clear differences in magnitude arranged in streaks can be seen here, which are structures stretched and parallel aligned in the streamwise direction. Kline et al. (1967) found from their investigations of turbulent boundary layers that these streaks are caused by rotating longitudinal vortices. The longitudinal vortices are self-maintaining in turbulent flows and draw the necessary energy from the main flow (Kim (2011)). By different directions of rotation of longitudinal-vortices lying alongside each other, fluid of higher velocity is either transported from the main flow into direction of the wall (*sweep*) or fluid transport of slow fluid away from the wall into direction of the main flow (*burst*) occurs. These mechanisms are shown in Fig. 7 (*bottom*). The practical relevance of these theoretical phenomena are shown in Fig. 7 (*middle*). Streamlines are used to visualize the global fluid movement in the area around the streaks. At areas of low wall shear stress, fluid is transported away from the wall in the direction of the main flow. By contrast, in areas with high wall shear stress, fluid of higher velocity is transported towards the wall. The influence of streaks on wall shear stress and thus on frictional drag has already been shown (Fröhlich (2006)). According to Kim (2011) longitudinal vortices are responsible for a considerable part of the wall friction. It is assumed that *sweep* in particular has a strong negative effect on friction resistance, as the transport of fluid with a high streamwise velocity to the wall increases the velocity gradient and thus also the wall shear stress which can be confirmed with the shown results of the presented LES.

Since the velocity and pressure ratios in the direct vicinity of the plate influence the wall shear stress and thus also the local frictional resistance, these are examined in detail below. Both Tay et al. (2015) and Nesselrooij et al. (2016) assume that the dimples produce secondary flows that are responsible for the effect of the dimple on the frictional resistance. Therefore, the flow in direct vicinity of the dimple by means of pressure and velocity analysis is considered. Due to the observed strong local variations in the quantities from dimple to dimple, measurements were taken on all dimples and averaged afterwards. In Fig. 8, the pressure distribution on the wall for the two arrangements studied is shown. The qualitative course of the related graphs is almost identical for both arrangements. For case OL, lower pressure values can be observed on the front and back of the dimple (indicated by dotted black lines) in both streamwise and spanwise direction. In streamwise direction the local maxima are approximately at the same level which leads to steeper pressure gradients for the OL arrangement. These are likely to be involved in loss generation, which is a possible reason for the lower resistance reduction of this arrangement. The pressure curve in spanwise direction is subject to higher local variations than in streamwise direction. This deviation is caused by local differences in flow velocity due to streaks. Nevertheless, the differences in the pressure characteristics are very small overall and do thus not allow for any concrete conclusions regarding the mechanisms of resistance influence of the dimples.

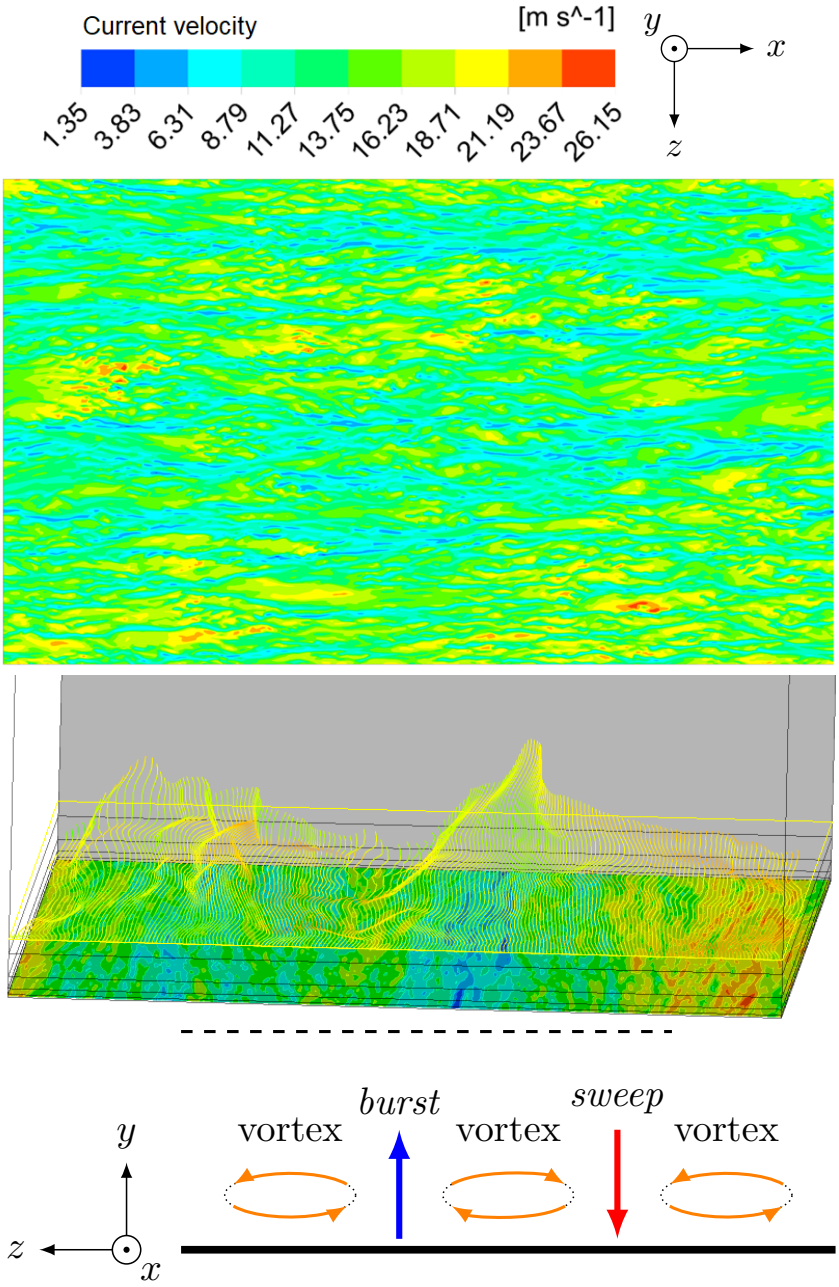

Figure 7: Streaks found as result of a LES visualised by velocity u in a section plane at $y^+ = 20$ (*top*), isometric view (flow approximately in direction of the drawing plane) with streamlines visualising *burst* and *sweep*, undimpled plate coloured by dimensionless wall shear stress, yellow line indicates the height of the starting points of the streamlines (*middle*) and schematic development of the streaks according to Kim (2003) (*bottom*)

3.3 Wall Shear Stress and Flow Velocity Perpendicular to the Wall

Fig. 9 shows the wall shear stresses τ_w in streamwise (x) and spanwise (z) direction on the surface for the dimpled arrangements OL and NOL as well as for the smooth reference channel. Here, a local increase in the wall shear stress in streamwise direction at the intake and a significant increase in shear stress at the end of the dimples can be observed for both dimpled plates. The entire curve and both peaks are higher for OL than for NOL, which fits very well with the overall higher observed c_F value for this arrangement. Also, most of the curve of the NOL arrangement is below the reference curve, which is also very well in accordance with the c_F values. This shows that the effects of drag reduction are related to the dimpled areas rather than the surrounding area of the dimples. The increase in wall shear stress at the entrance of a dimple can be attributed to acceleration of fluid in these areas (Isaev et al. (2010)). The subsequent strong decrease right behind it indicates that flow can follow the wall within

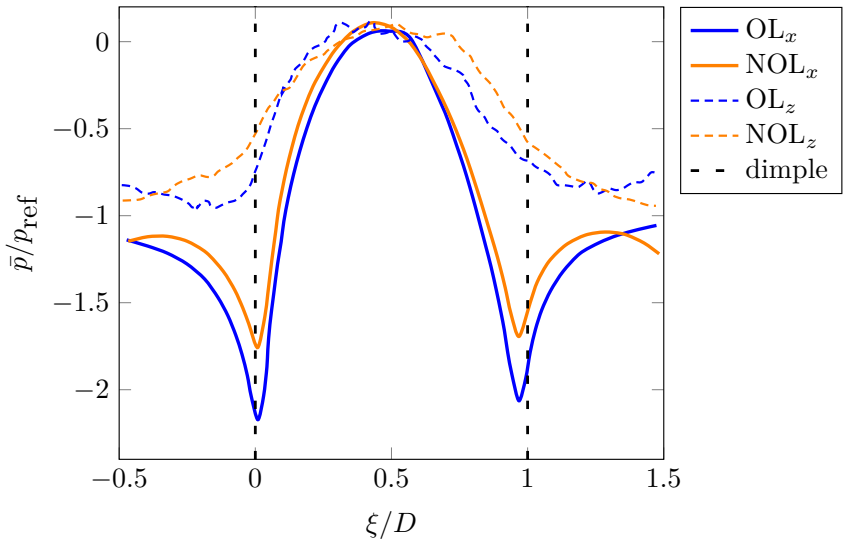

Figure 8: Static pressure at the dimpled wall in direct proximity of the dimples

that area only limitedly. Since the values remain above 0, there is no flow separation as would be the case with dimples of higher h/D. Such a detachment would increase the form resistance and is thus to be avoided (Tay et al. (2015)). The wall shear stresses in spanwise direction show a locally fluctuating but comparable course for all three cases. Fluctuations show the influence of the streaks and the resulting secondary currents close to the wall. The wall shear stress in this direction is not influenced by the dimples.

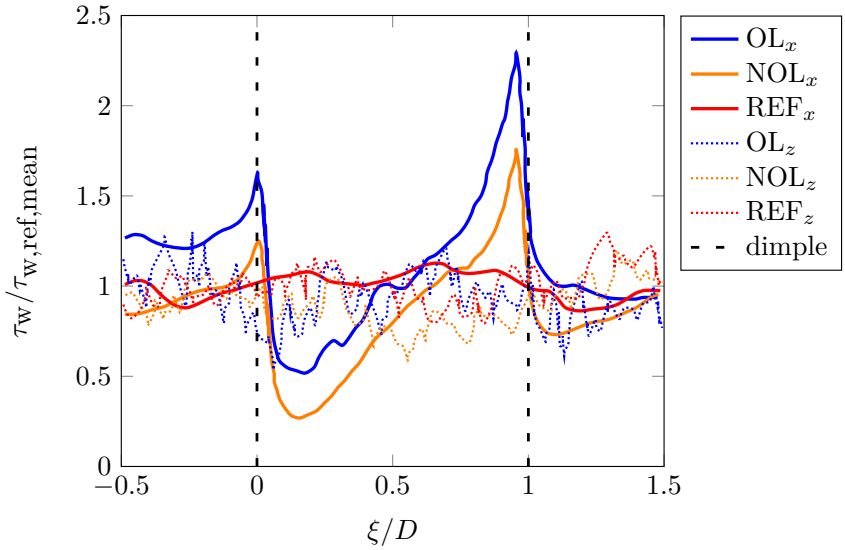

Figure 9: Normalized τ_{w} in streamwise (x) and spanwise (z) direction for the plate without dimples (REF), plate with overlapping dimple arrangement (OL) and plate with non-overlapping dimple arrangement (NOL) in direct proximity of the dimple

In order to examine the velocity distribution around the dimples, these were evaluated over five measuring points as depicted in Fig. 1 (*middle*). For this purpose, the velocity components u, v and w along lines in the y-direction and starting from the measuring points were analysed. In this case too, the evaluation was performed for all dimples and the values were averaged afterwards. The y-component (v) of fluid velocity proved to be of particular interest here because the most significant differences occurred between the configurations OL and NOL. Since the influence of the dimples is particularly pronounced near the wall, but the velocity components on the wall due to the no-slip condition are 0, the range $10 \leq y^+ \leq 800$ is shown in Fig. 10. It can be seen that above point 3, i. e. in the middle of the dimple, the mean wall-normal velocity component over the entire boundary layer is oriented in the direction of the wall. This is due to the expansion of the flow cross-section by the dimple. It is interesting to note that above the lateral borders of the dimples (points 2 and 4) the values for v for the arrangement NOL are clearly

more symmetrical around the zero line than for the arrangement OL. This means that the streaks in arrangement NOL are much better aligned with the dimples. This observation suggests that this stabilization of the streaks can have a positive effect on the flow resistance if the intensity of the streaks is kept low.

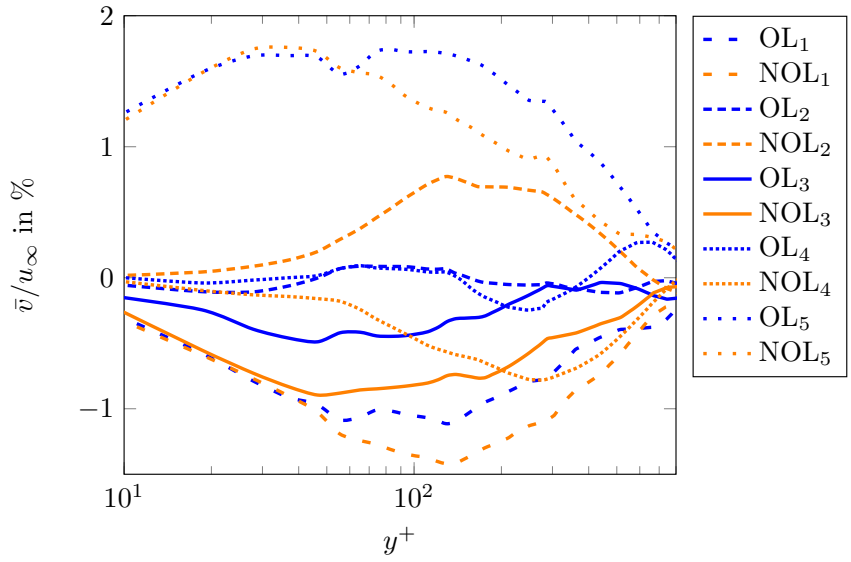

Figure 10: Average velocity $\bar{v}$ perpendicular to the wall scaled with bulk velocity u_∞ for the overlapping (OL) and non overlapping (NOL) arrangements at different physical positions 1–5 inside a dimple as indicated in Fig. 1

4 Conclusion

In this paper, two different arrangements of dimples on a plate were investigated numerically via Large Eddy Simulations with respect to their drag reduction potential. It was found that, in absolute terms, the results were consistent with available literature values for these setups, but only a minimal resistance reduction of 0.12 % could be achieved with one setup, while a reduction of 3.16 % was possible with the other. According to literature, however, the first case should have resulted in higher drag reduction while the second case should have resulted in a slight increase in resistance. Investigation of the flow structures in the immediate vicinity of the dimples revealed that the setup with higher drag reduction also showed lower wall shear stresses locally in the area of the dimples. The analysis of wall normal velocity also suggested that in this case existing longitudinal vortices can be stabilized. Even if these longitudinal vortices can have negative effects on flow resistance, these results lead to the assumption that a stabilization of the vortices by dimples is possible and advantageous. In order to investigate this assumption further, there is a need for additional investigations in this area. A time-resolved comparison of the local resistance components with the associated flow phenomena due to dimples would be of particular interest.

References

Antonia, R. A.; Spalart, P. R.; Mariani, P.: Effect of suction on the near-wall anisotropy of a turbulent boundary layer. *Physics of Fluids*, 6, 1, (1994), 430–432.

Baron, A.; Quadrio, M.: Turbulent drag reduction by spanwise wall oscillations. *Applied Scientific Research*, 55, 4, (1996), 311–326.

Cimarelli, A.; Frohnapfel, B.; Hasgawa, Y.; de Angelis, E.; Quadrio, M.: Prediction of turbulence control for arbitrary periodic spanwise wall movement. *Physics of Fluids*, 25, 075102.

Fröhlich, J.: *Large Eddy Simulation Turbulenter Strömungen*. B. G. Teubner Verlag, 1 edn. (Sep. 2006).

Garcia-Mayoral, R.; Jimenez, J.: Drag reduction by riblets. *Philosophical Transactions of the Royal Society A: Mathematical, Physical and Engineering Sciences*, 369, (2011), 1412–1427.

Herwig, H.; Schmandt, B.: *Strömungsmechanik*. Springer Vieweg, 3 edn. (2015).

Isaev, S.; Kornev, N.; Leontiev, A.; Hassel, E.: Influence of the reynolds number and the spherical dimple depth on turbulent heat transfer and hydraulic loss in a narrow channel. *International Journal of Heat and Mass Transfer*, 53, 1-3, (2010), 178–197.

Kiknadze, G. I.; Gachechiladze, I. A.; Barnaveli, T. T.: The mechanisms of the phenomenon of tornado-like jets self-organization in the flow along the dimples on the initially flat surface. In: *Proceedings of the ASME 2012 International Mechanical Engineering Congress & Exposition*, vol. 7, pages 3017–3026, ASME (Nov. 2012).

Kim, J.: Control of turbulent boundary layers. *Physics of Fluids*, 15, 5, (2003), 1093–1105.

Kim, J.: Physics and control of wall turbulence for drag reduction. *Philosophical Transactions of the Royal Society A: Mathematical, Physical and Engineering Sciences*, 369, 1940, (2011), 1396–1411.

Kiš, P.; Jin, Y.; Herwig, H.: The physics of stripe patterns in turbulent channel flow determined by DNS results (2015), arXiv:1511.07753.

Kline, S. J.; Reynolds, W. C.; Schraub, F. A.; Runstadler, P. W.: The structure of turbulent boundary layers. *Journal of Fluid Mechanics*, 30, 4, (1967), 741–773.

Krieger, V.; Perić, R.; Jovanović, J.; Lienhart, H.; Delgado, A.: Toward design of the antiturbulence surface exhibiting maximum drag reduction effect. *Journal of Fluid Mechanics*, 850, (2018), 262–303.

Kühnen, J.; Song, B.; Scarselli, D.; Budanur, N. B.; Riedl, M.; Willis, A. P.; Avila, M.; Hof, B.: Destabilizing turbulence in pipe flow. *Nature Physics*, 14, (2018), 386–390.

Lashkov, Y. A.; Samoilova, N.: On the viscous drag of a plate with spherical recesses. *Fluid Dynamics*, 37, 2, (2002), 231–236.

Lienhart, H.; Breuer, M.; Köksoy, C.: Drag reduction by dimples? - A complementary experimental/numerical investigation. *International Journal of Heat and Fluid Flow*, 29, (2008), 783–791.

Moser, R. D.; Kim, J.; Mansour, N. N.: Direct numerical simulation of turbulent channel flow up to $Re_\tau = 590$. *Physics of Fluids*, 11, 4, (1999), 943–945.

Nesselrooij, M. v.; Veldhuis, L. L. M.; Oudheusden, B. W. v.; Schrijer, F. F. J.: Drag reduction by means of dimpled surfaces in turbulent boundary layers. *Experiments in Fluids*, 57, 142, (2016), 1–14.

Nicoud, F.; Ducros, F.: Subgrid-scale stress modelling based on the square of the velocity gradient tensor. *Flow, Turbulence and Combustion*, 62, (1999), 183–200.

Park, H.; Lee, D.; Jeong, W.-P.; Hahn, S.; Kim, J.; Kim, J.; Choi, J.; Choi, H.: Drag reduction in flow over a two-dimensional bluff body with a blunt trailing edge using a new passive device. *Journal of Fluid Mechanics*, 563, (2006), 389–414.

Park, J.; Choi, H.: Effects of uniform blowing or suction from a spanwise slot on a turbulent boundary layer flow. *Physics of Fluids*, 11, 10, (1999), 3095–3105.

Quadrio, M.; Ricco, P.: Critical assessment of turbulent drag reduction through spanwise wall oscillations. *Journal of Fluid Mechanics*, 521, (2004), 251–271.

Sirovich, L.; Karlsson, S.: Turbulent drag reduction by passive mechanisms. *Nature*, 388, (1997), 753–755.

Tay, C. M.: Determining the effect of dimples on drag in a turbulent channel flow. In: *49th AIAA Aerospace Sciences Meeting including the New Horizons Forum and Aerospace Exposition AIAA 2011-682 4 – 7 January 2011, Orlando, Florida* (Jan. 2011).

Tay, C. M. J.; Khoo, B. C.; Chew, Y. T.: Mechanics of drag reduction by shallow dimples in channel flow. *Physics of Fluids*, 27, 035109.

Turow, J.: *Flow structures and heat transfer on dimpled surfaces*. phdthesis, University of Rostock (2012).

Veldhuis, L. L. M.; Vervoort, E.: Drag effect of a dented surface in a turbulent flow. In: *27th AIAA Applied Aerodynamics Conference AIAA 2009-3950 22 - 25 June 2009, San Antonio, Texas* (Jun. 2009).

Address: Institute for Factory Automation and Production Systems, Faculty of Engineering, Friedrich-Alexander-University Erlangen-Nuremberg. Fürther Straße 246b, 90429 Nuremberg, Germany.
email: `Julian.Prass@faps.fau.de`